

RANS CFD simulation for slender floating bodies with forward speed and comparison to BEM with uniform-flow approximation

Farid P. Bakti* and MooHyun Kim

Department of Ocean Engineering, Texas A&M University, College Station, Texas, USA

(Received April 23, 2021, Revised May 24, 2021, Accepted May 26, 2021)

Abstract. The nonlinear wave-uniform current interaction for a slender floating body is investigated by using the commercial CFD (computational fluid dynamics) tool STAR-CCM+ and author-developed simplified BEM (boundary element method) based on potential theory and perturbation approach. The STAR-CCM+ solves the fully non-linear Reynold Averaged Navier Stoke's (RANS) equation for real fluid in the finite volume framework. The viscous effect is accounted for by mesh refinement and the $k - \omega$ turbulence closure model. Meanwhile, the fully non-linear body motion and free surface elevation are considered by the overset mesh and volume of fluid method, respectively. Two different input waves with different order of non-linearity are compared to see their effects on ship's motion and added resistance. A detailed step-by-step simulation setup is explained to ensure the reproducibility of the results. Several preliminary simulations such as static tank test, wave calibration, and towing tank case are also conducted for quality assurance. The CFD results show good agreements with both the BEM with Uniform Flow approximation (UF-BEM) and the experimental data by other researchers when the λ/L is large. The CFD simulation also shows that it can properly capture the second-order force (added resistance) and highly non-linear motion with breaking waves close to the pitch resonance frequency. However, the CFD simulation requires substantially higher computational cost than the UF-BEM. The comparison study shows that the UF-BEM can produce reasonably good results for practical applications with significantly less computational time and human effort. On the other hand, the CFD program can be used for proof computations for special cases.

Keywords: CFD; BEM; Navier-Stokes equation; fluid-structure interaction; fully non-linear; wave-current interaction; forward speed; added resistance

1. Introduction

Computational Fluid Dynamics (CFD) is well known for its capabilities for solving non-linear fluid-structure interactions. Although several alternatives, such as the non-linear boundary element method (BEM), are also capable of simulating highly non-linear phenomena (i.e., Celebi *et al.* 1998, Kim and Koo 2019), they still assume non-breaking waves and inviscid fluids. On the contrary, the CFD method can solve fully non-linear fluid-structure interactions with viscous effects and breaking waves (Jiao and Huang 2020, Bandringa and Helder 2020, Heilskov and Peterson 2016). The viscous effects are typically crucial when flow separation occurs, such as the case of oblique current loads acting on FPSOs (Arjen *et al.* 2020). Another example of high viscous effects is the roll damping

*Corresponding author, Ph.D. Student, E-mail: faridputrabakti@gmail.com

provided by ship's bilge keel (Irkal *et al.* 2016). However, for mild sea conditions with small wave-heading angle, the force and motion are typically pressure dominated, so the inviscid-fluid assumption can still be used in the CFD simulation to save computational time, as was shown by (Vigsnes 2018).

In this study, a free-surface problem is considered where a non-mixing two-phase flow (water and air) involving a sharp interface boundary is modeled. In general, there are two different CFD frameworks in solving the free-surface problems. The first is the Eulerian framework (e.g., VOF; volume of fluid method), and the second is the Lagrangian framework (e.g., SPH; smoothed particle hydrodynamics). The Lagrangian approach typically has a straightforward interface definition and can deal with a violent free-surface flow with relative ease. However, this method typically requires a considerable computing effort since the resolution is generally kept the same throughout the domain (no local refinement). Furthermore, the particle position in the Lagrangian method changes at each time step (Bakti *et al.* 2016).

Many studies showed that correctly modeled Eulerian CFD methods produced reliable results for wave's radiation-diffraction problems. For instance, (Jin *et al.* 2017) showed a good agreement between the CFD and experimental results for head and oblique waves with zero forward speed. The CFD also showed reliable results for seakeeping problems for moderate Froude number $0.1 < F_n < 0.25$ as presented in (Orihara 2011, Islam *et al.* 2019, Sadat-Hosseini 2013). These studies simulated various loading conditions for short and long waves from various directions. More complicated loading conditions were investigated in (Jiao & Huang, 2020), where bi-directional seas were considered in the seakeeping analysis. In (Wu 2011), a high speed ($F_n = 0.7$) trimaran vessel was simulated. Despite its versatility, the typical RANS CFD methods require many numerical tuning parameters and intensive human effort to set them up. Several efforts led by the industry were made to standardize the best practice in simulating practical engineering problems by using CFD tools (Arjen *et al.* 2020, Bouscasse *et al.* 2020). In this study, a detailed step-by-step explanation is given on how to properly set up the CFD parameters for the simulations of a floating body with forward speed (or in uniform current).

The wave-body-uniform flow interaction problems can also be resolved through lower-cost alternatives, such as the potential theory with BEM. Unlike the typical RANS CFD method, the BEM method only requires the equations to be solved at the boundaries, thus significantly reducing the computational requirement. When combined with the Neumann-Kelvin (or Uniform Flow) approximation (Ogilvie and Tuck 1969, Salvesen *et al.* 1970, Brard 1972), the UF-BEM was shown to be able to provide meaningful first-cut results for slender floating body with relatively low forward speed (Beck and Loken 1989, Papanikolaou and Schellin 1992, Guha and Falzarano 2015, Guha and Falzarano 2016). In this study, an in-house BEM code with Uniform Flow approximation (UF-BEM) is developed and the results are compared against the fully non-linear CFD methods. The comparison also indirectly measures the effectiveness of the method in terms of accuracy and computational cost. From these measures, we can then suggest the best engineering practice to maximize the value of both the BEM-UF and CFD simulation tools.

2. Methodology

2.1 Computational fluid dynamics

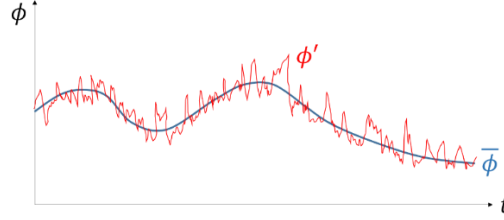


Fig. 1 Variables description in RANS formulation

2.1.2 Reynold Averaged Navier-Stokes (RANS) and turbulence closure model

A commercial CFD software Star-CCM+ is used to model the fully non-linear fluid-structure interaction. Star-CCM+ software is capable of solving the RANS problem using the Finite Volume Method. In the RANS model, fluctuating field variables, e.g., ϕ , can be represented as a mean value and its perturbation i.e.

$$\phi = \bar{\phi} + \phi' \quad (1)$$

where $\bar{\phi}$ is the average value of ϕ over a particular time or spatial scale, and ϕ' is the perturbation along $\bar{\phi}$, as illustrated in Fig. 1.

Substituting Eq. (1) into the mass, momentum, and energy conservation equations, the governing equations for the RANS problem are written as

$$\frac{\partial \rho}{\partial t} + \nabla \cdot (\rho \bar{\mathbf{v}}) = 0 \quad (2)$$

$$\frac{\partial(\rho \bar{\mathbf{v}})}{\partial t} + \nabla \cdot (\rho \bar{\mathbf{v}} \otimes \bar{\mathbf{v}}) = -\nabla \cdot (\bar{p} \mathbf{I}) + \nabla \cdot (\bar{\mathbf{T}} + \mathbf{T}_{RANS}) + \mathbf{f}_b \quad (3)$$

$$\frac{\partial(\rho \bar{E})}{\partial t} + \nabla \cdot (\rho \bar{E} \bar{\mathbf{v}}) = -\nabla \cdot (\bar{p} \mathbf{I}) \bar{\mathbf{v}} - \nabla \cdot (\bar{\mathbf{T}} + \mathbf{T}_{RANS}) \bar{\mathbf{v}} + \mathbf{f}_b \cdot \bar{\mathbf{v}} + S_E \quad (4)$$

where \otimes is the outer product operator, ρ is the fluid density per unit volume, \mathbf{v} is the velocity vector, p is the pressure, \mathbf{I} is the identity matrix, \mathbf{f}_b is the resultant body force (such as gravity or centrifugal force), S_E is the energy source per unit volume, and \mathbf{T} is the viscous or shear stress tensor. By employing the Boussinesq hypothesis where the small scale turbulent stress \mathbf{T}_{RANS} is assumed to be linearly proportional to the large scale mean stress \mathbf{T} (i.e., $\overline{u'_x u'_y} \sim \frac{1}{2} \left(\frac{\partial \bar{u}_x}{\partial y} + \frac{\partial \bar{u}_y}{\partial x} \right)$), the turbulent Reynold stress tensor \mathbf{T}_{RANS} formula can be written as

$$\mathbf{T}_{RANS} = \rho \nu_T \begin{bmatrix} 2 \left(k_{TE} / \nu_T + \frac{\partial \bar{u}_x}{\partial x} \right) & \left(\frac{\partial \bar{u}_x}{\partial y} + \frac{\partial \bar{u}_y}{\partial x} \right) & \left(\frac{\partial \bar{u}_x}{\partial z} + \frac{\partial \bar{u}_z}{\partial x} \right) \\ & 2 \left(k_{TE} / \nu_T + \frac{\partial \bar{u}_y}{\partial y} \right) & \left(\frac{\partial \bar{u}_y}{\partial z} + \frac{\partial \bar{u}_z}{\partial y} \right) \\ \text{Sym} & & 2 \left(k_{TE} / \nu_T + \frac{\partial \bar{u}_z}{\partial z} \right) \end{bmatrix} \quad (5)$$

where k_{TE} and ν_T are the turbulent kinetic energy and turbulent eddy viscosity, respectively. Different from the fluid's kinematic viscosity, ν_T is a flow property that highly dependent on the flow condition itself. Several different closure models are developed to provide constitutive relations

to solve the turbulent eddy viscosity and turbulent kinetic energy. According to recent development on the standard CFD practice in the industry (Bouscasse *et al.* 2020), $k - \omega$ is the preferred choice of turbulence model when dealing with minimum flow separation and no eddy detachment in marine application involving free surface waves. In summary, the $k - \omega$ model solves for eddy viscosity ν_T by solving the transport equations of two turbulence related variables: the turbulent kinetic energy k_{TE} and the dissipation rate per unit kinetic energy ω_{TE} . The detailed derivation, validation, and comparative study of the $k - \omega$ model can be found in (Wilcox 1998).

Close to the wall boundary, the viscous force is at least of the same magnitude as the inertial force. This so-called boundary layer is not considered in the potential theory. However, it plays a vital role in several fluid-structure interaction problems. In marine applications, the viscous effect such as turbulence, skin drag, and vortex shedding provides additional forcing or damping. For example, in a ship's roll resonance motion where wave-making damping is small, the motion is largely affected by the viscous damping (Irkal *et al.* 2016). To properly account for these flow separations and viscous shear stress due to the boundary layer effect, high resolution close to the non-slip surface is needed. To calculate the boundary layer thickness, non-dimensional distance and velocity are introduced as follows (White 2006)

$$y^+ = \frac{u^* y}{\nu} \quad (6)$$

$$u^* = \sqrt{\tau_w / \rho} \quad (7)$$

where u^* , τ_w , and ν , are the wall friction velocity, wall shear stress, and the fluid's viscosity, respectively. The symbol y^+ is a non-dimensional distance from the wall that divides the boundary layer regions into the viscous ($y^+ < 5$), buffer ($5 < y^+ < 30$), inertial ($30 < y^+ < 200$), and outer layers ($y^+ > 200$). The shear stress can be calculated by its relation to the skin friction coefficient \bar{C}_f . The skin friction coefficient \bar{C}_f is approximated as follows (Adapco 2020)

$$\bar{C}_f = \frac{2\tau_w}{\rho \bar{U}^2} \quad (8)$$

$$\bar{C}_f \cong \frac{0.066}{(\log Re - 2.03)^2} \quad (9)$$

where Re is the Reynold number, defined as $Re = \rho \bar{U} L_x / \mu$, \bar{U} is the ambient or averaged fluid's velocity, and L_x the is the arclength of the non-slip wall boundary.

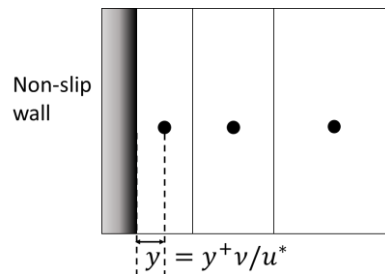


Fig. 2 First cell definition with regard to the computed y value

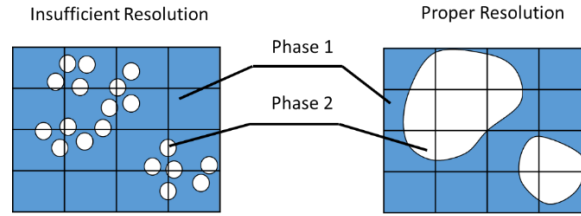


Fig. 3 Grid requirements in VOF method

The first cell's centroid location can then be calculated by substituting Eq. (7) into Eq. (6) and by choosing the appropriate value of y^+ that we want to resolve. In marine application without any significant flow separation, (Bouscasse 2020) suggested that the first cell height has to sufficiently resolve y^+ value of < 10 . The first cell height can then be determined to be twice the y value computed from Eq. (7) as shown in Fig. 2.

2.1.3 Free surface tracking method

Free-surface flow is considered as a non-mixing two-phase flow involving a sharp interface between a heavy fluid (water) and light fluid (air). In this study, the volume of fluid (VoF) method is chosen to track the interface with minimum computation cost. In the VoF method, volume fraction $\alpha_i = \mathcal{V}_i / \mathcal{V}_{cell}$ is used to describe the distribution of phases and the location of the interface, with \mathcal{V}_i defined as the volume of phase i located inside a cell with a volume of \mathcal{V}_{cell} . The summation of the volume fractions of all phases in a cell should be equal to one. In two-phase fluid flow, the interface location is located where $\alpha_i = 0.5$ for any i . The volume fraction is then applied to the governing transport equation Eqs. (2)-(4) as a multiplication factor. A detailed description of the VoF method can be found in (Muzaferija and Peric 2017).

The free surface tracking using the VoF approach requires high mesh resolution in the interface region to resolve the interface position and shape, as illustrated in Fig. 3. Considering this, free surface mesh refinement is needed to adequately capture the wave's height (H) and wavelength (λ). According to STAR-CCM+ guidelines, the typical value of $\lambda/dx = 80-120$ and $H/dz = 15-40$ is needed in the free surface region.

2.1.4 Boundary and initial condition

The illustration of the boundary conditions in the present computational domain can be found in Fig. 4. The velocity-inlet boundary is used for upstream, top, and side boundaries, where the x-y-z velocity components are set to match the theoretical input-wave velocity. A pressure outlet is used for the downstream boundary, where the pressure is set to match the theoretical wave's hydrostatic pressure considering fluctuating free surface. This is further explained in the next section. We used the symmetry plane boundary condition at the horizontal half-plane to reduce the computational domain by half. No-slip wall boundary is used at the bottom boundary and ship's hull, where the boundary layer theory is applied to these boundaries. A special type of boundary called the overset mesh boundary is used at a small control volume enclosing the hull and some part of the fluid domain.

Overset mesh (also called the chimera grid method) discretizes the computational domain into several meshes that overlap each other in an arbitrary manner (Adapco 2020). The overset method is suitable for problems with large relative motions because it does not need to regenerate the mesh

throughout the whole computation domain at every time step. With this method, only local mesh cutting and regeneration around the enclosed foreground region is needed (see Figs. 4 and 5 for the definition of foreground region). Furthermore, most overlapping meshes are only solved in the foreground region, while the same mesh in the background region is excluded in the calculation through mesh hole cutting. The hole cutting region and cell type in a typical seakeeping analysis can be found in Fig. 5, while detailed information and formulations used in the overset mesh can be found in (Hadzic 2005).

The Airy (1st order) and Stokes (5th order) wave’s free surface position, fluid’s velocity and pressure are used as the boundary and initial values throughout the simulation. The wave tank is set so that the deepwater condition is satisfied $d/\lambda > 0.5$. The volume fraction of the fluid can be found from the sea level position η by employing the level set function (Bihs 2016) as follows

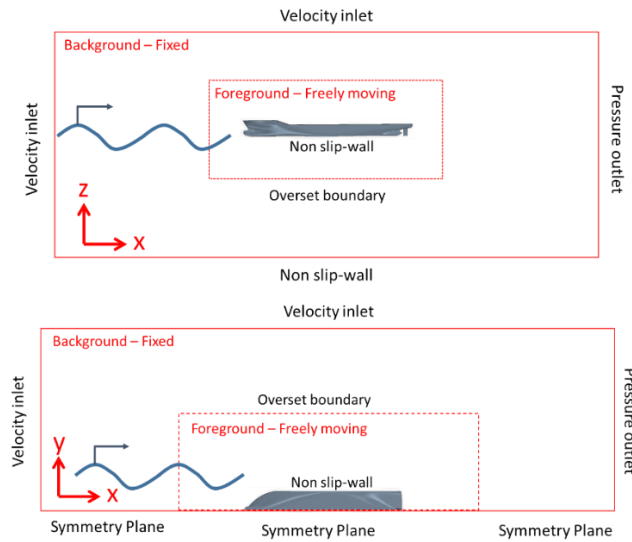


Fig. 4 Boundary conditions

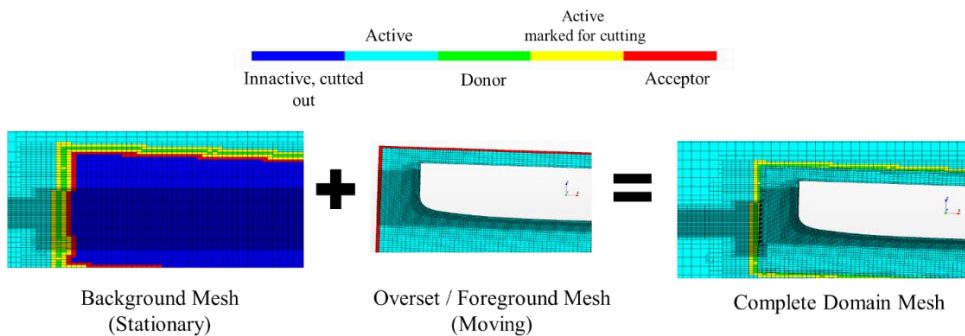


Fig. 5 Overset mesh cell type

$$\alpha_i = \alpha_1 H(\eta^*) + \alpha_2 (1 - H(\eta^*)) \quad (10)$$

$$H(\eta^*) = \begin{cases} 0 & \text{if } \eta^* < -\epsilon \\ \frac{1}{2} \left[1 + \frac{\eta^*}{\epsilon} + \frac{1}{\pi} \sin\left(\frac{\pi\eta^*}{\epsilon}\right) \right] & \text{if } |\eta^*| < \epsilon \\ 1 & \text{if } \eta^* > \epsilon \end{cases} \quad (11)$$

Where $\eta^* = (\eta - z)$ and $\epsilon = 1.6dz$.

2.1.5 Wave forcing zone

The theoretical wave values are forced at the boundaries mentioned above. Because of this, the wave's reflection and flow discontinuity might occur, especially at the pressure outlet and velocity inlet. This phenomenon can be avoided by introducing the wave forcing zone. The wave forcing zone enforced the momentum equation (velocity values) over a bounded region of the computational domain to follow the predefined theoretical values by using the Euler overlay method (Kim *et al.* 2012). In the Euler overlay method, the following additional forcing term is added to the momentum conservation equation

$$q_\phi = -\gamma_{wz}\rho(\phi - \phi^*) \quad (12)$$

where q_ϕ , γ_{wz} , ϕ , and ϕ^* is the momentum forcing term, forcing coefficient, current solution of the transport equation, and predefined theoretical value which the solution is forced towards. The forcing coefficient γ_{wz} is chosen to be monotonically increasing from the edge of the wave forcing zone to its maximum value at the boundary. In STAR-CCM+, the cosine function is used as the forcing coefficient as follow

$$\gamma_{wz} = -\gamma_0 \cos^2\left(\frac{\pi x}{2L_{wz}}\right) \quad (13)$$

where γ_0 and L_{wz} are the wave forcing coefficient and wave zone distance from the boundary, respectively. Depending on the length of the wave zone and the flow characteristics, γ_0 is typically chosen to be a large value ($\gamma_0 > 10$). We found that when the wave zone distance is set to be $L_{wz} < 2\lambda$, the waves with smaller wavelength require higher γ_0 compared to that of a longer wavelength. In this study, L_{wz} is chosen to be $\lambda < L_{wz} < 2\lambda$ at the downstream boundary and $0.5\lambda < L_{wz} < \lambda$ at the upstream and side boundaries. Forcing coefficient of $50 < \gamma_0 < 150$ is used in this study.

2.1.5 Fluid-body Interaction

The Dynamic Fluid Body Interaction (DFBI) models solve for the rigid-body motion of an object exposed to surface forces (e.g., shear and pressure from fluid) as well as body forces (e.g., gravity). DFBI calculates the resultant forces and moments acting on the selected wall boundaries and then updates the body's new position at each inner iteration step until convergence is reached. The equations of translational and rotational motions are given by

$$m \frac{\partial v}{\partial t} = \mathbf{F} \quad (14)$$

$$\mathbf{I} \frac{\partial \boldsymbol{\omega}}{\partial t} + \boldsymbol{\omega} \times \mathbf{I} \boldsymbol{\omega} = \mathbf{M} \quad (15)$$

where m is the body mass, \mathbf{I} is the mass moment of inertia tensor, and $\boldsymbol{\omega}$ is the rotation vector.

The external force vector \mathbf{F} and moment vector \mathbf{M} are calculated by integrating the stresses over the body's surface. Combined with the overset mesh, the DFBI solver provides a robust tool to solve the fully non-linear fluid-body interaction.

For steady flow analysis, such as towing tank simulation, the motion solver can be frozen for several time steps until the predetermined convergence criteria are met. After that, the body is moved to a new position, and the same step is repeated until the change of the body's position is negligible. This quasi-static approach can significantly reduce the computational cost in the steady flow analysis and was used in our uniform-flow-only simulation.

2.1.6 Time stepping, computational domain, and meshing

A second-order implicit unsteady scheme is recommended for free surface flow with a sharp interface (Vignès 2018). The stability Courant–Friedrichs–Lewy (CFL) stability requirement of the second-order scheme is higher than that of the first-order scheme. However, it can properly propagate the free surface with minimum numerical dissipation. The following time-stepping criteria are used to reduce the computational cost while maintaining numerical stability:

1. Stopping the inner iteration within one time step and go to the next time step when one of the following conditions are met:
 - Volume fraction residual < 0.001
 - Momentum residual < 0.001
 - Continuity residual < 0.1
 - 15 iteration is reached
2. Setting reference / initial time step value to be the minimum value of the following criteria:
 - $\Delta t = T/(4.8N_x)$: To properly capture the wave's behavior at each period. Where T is the wave's period, and N_x is the number of cells per wavelength
 - $\Delta t = 0.5\Delta x_{min} \max(C_g, [U + |\mathbf{v}|])$: from CFL requirement to restrict the flow so that it only propagates half the smallest cell size (Δx_{min}). Where C_g is the wave's group velocity, U is the uniform flow speed, and $|\mathbf{v}|$ is the magnitude of the wave's particle velocity.
3. The built-in automatic adaptive time step is set to keep the maximum instantaneous CFL number < 0.54 . Also, the minimum allowable time step is set to be 10^{-3} of the reference time step from point number 2.

The computational domain needs to be large enough to incorporate the wave forcing region without significantly changing the free surface profile close to the body. Furthermore, it needs to be large enough so that the body's local flow field perturbation does not reach the boundaries to avoid reflection. The water depth also needs to be deep enough ($d > 0.5\lambda$) so that deep water assumption can be maintained. However, the computational domain needs to be kept as small as possible to reduce the computational cost. Considering all of the above, the computational domain size is kept at a particular ship and wavelength ratio, as illustrated in Fig. 6.

To properly capture the free surface and non-linear body motion, mesh refinements are applied to certain vital regions, as shown in Fig. 7. In summary, the objectives of the mesh refinement regions are as follows:

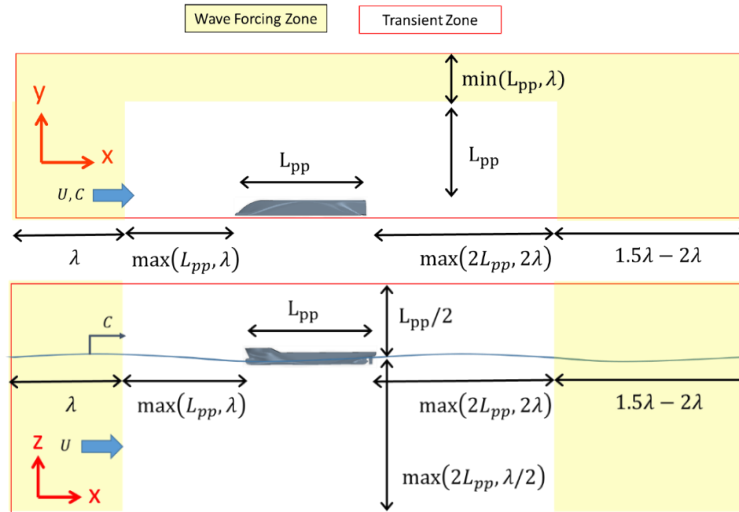


Fig. 6 Computational domain

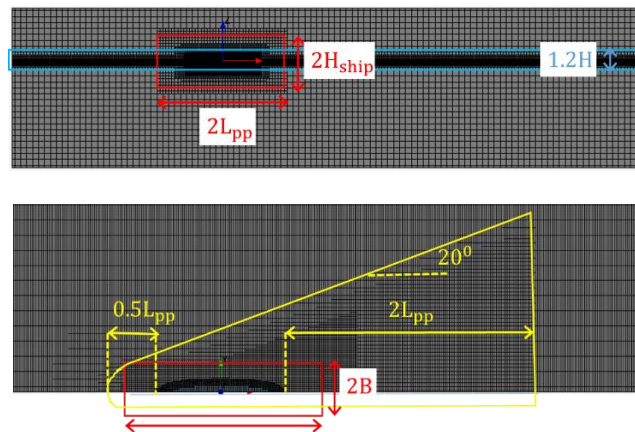


Fig. 7 Mesh refinement regions

- Free surface refinement (blue line): To adequately capture the incoming, diffracted, and radiated wave's interface. Since the body is streamlined in the head-sea condition, the refinements are only done in x and z directions (see VoF subsection for details)
- Wake refinement (yellow line): To adequately capture the steady ship waves (Kelvin wave). Since the waves are radiated outward from the body within 20° angle, the refinements are done in x and y direction, while the z refinement follows the free surface refinement
- Near-overset boundary refinement (red line): To provide sufficient interpolation cells for the overset mesh and to resolve local perturbation such as the bow and stern waves and wave run-up close to the body (see overset and VoF subsection for details)

2.2 Frequency domain BEM with UF approximation

Potential theory for inviscid, incompressible, irrotational flow is used to solve the wave-uniform flow interaction problem with minimum computational cost. In the potential theory, Laplace equation is used as the governing equation. In the steady Kelvin ship wave problem, Brard (1972) considers a linearized free surface condition where the steady perturbation can be considered small. Therefore its multiplication can be neglected by considering small uniform flow or slender body ($\partial/\partial x \ll \partial/\partial y$ or $\partial/\partial z$). Using the same assumptions, Salvesen *et al.* (1970) then proposed a wave-uniform flow interaction solution where the multiplication between the steady perturbation and the unsteady potential can be neglected (e.g., in the body boundary condition). By considering the linearized boundary value problem, the complexity of the problem is significantly reduced. This so-called Neumann-Kelvin problem is referred to as the uniform flow (UF) approximation in this study due to the lack of steady perturbation in the final formulation. Two of the most significant consequences of the UF approximation in the linear problems can be found in the free surface (Eq. (16)) and body (Eq. (17)) boundary conditions.

$$\left[\mathbf{g} \frac{\partial}{\partial z} + \left(\frac{\partial}{\partial t} - U \frac{\partial}{\partial x} \right)^2 \right] \phi_w = 0 \quad \text{on} \quad \text{free surface} \quad (z = 0) \quad (16)$$

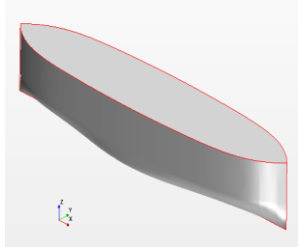
$$\phi_{rk} = \begin{cases} \phi_{rk}^0 & \text{for } k < 5 \\ \phi_{rk}^0 + U\phi_{rk}^0 & \text{for } k = 5 \\ \phi_{rk}^0 - U\phi_{rk}^0 & \text{for } k = 6 \end{cases} \quad \text{on} \quad \text{body surface} \quad (17)$$

where ϕ_w is the total wave potential consisting of the radiation potential $\phi_R = \sum_{k=1}^6 \eta_k \phi_{rk}$ and the diffraction potential ϕ_D . η_k and U are the generalized body motion vector and uniform flow magnitude, respectively. The superscript zero on the radiation potential marks the solution without considering the uniform flow.

The linearized boundary value problem is then solved using the boundary element method (BEM) in the frequency domain, with the free-surface Green's function. The BEM method uses a Green's function that satisfies all the boundary conditions, except that on the body boundary, which is problem specific. Thus, the free surface Green function significantly reduces computational requirement since the discretization is only needed on the body boundary. With additional assumptions, the uniform flow effect can be readily calculated from the zero speed results. Therefore, the UF method can be implemented as a post-processing tool to any fluid-structure interaction simulation code. However, for non-linear problems such as the added resistance problem, the UF method is not straightforward, as shown in Kim and Kim (2010), Guha and Falzaro (2015), and Bakti and Kim (2020).

An in-house frequency domain BEM with UF approximation is used for comparison with the CFD simulation. The complete derivation and formulation for the diffraction forces, added mass, hydrodynamic damping, equation of motion, and the added resistance of the UF-BEM method can be found in Salvesen *et al.* (1970), Papanikolaou and Schellin (1992), Guha and Falzarano (2016), and Bakti *et al.* (2021).

Table 1 Hull's Particulars

Hull Shape	Item	Notation	Value	Unit
	Length	L	5	m
	Breadth	B	1	m
	Total Depth	h_{bm}	0.85	m
	Draft	d	0.35	m
	Displaced Volume	∇	1.109	m ³
	Vertical CoG	KG	0.062	m
	y - Radii of Gyration	r_{yy}/L	0.236	m

3. Case definition

Modified blunt Wigley hull as defined in Table 1 is used as a case study. This hull is similar to the blunt Wigley hull used in Kashiwagi (2013) with a 1:2 Froude scaling ratio. Furthermore, the hull is extended vertically upward from the water line to reach the desirable total height so that the wave run-up can be properly accounted for. To validate all of the body's input (e.g., displaced volume, inertia, the center of gravity), we first did the hydrostatic test with a freely floating body.

Table 2 CFD simulation cases

Case Name	F_n	H (m)	λ (m)	T_e (sec)	Body	Wave Tank	Wave's Order
Tow	0.2	N/A	N/A	N/A	Yes	Tank0	N/A
Wave1_Only	0.0	0.3	10	2.53	No	Tank1	1 st
Wave1_Mot0	0.0	0.3	10	2.53	Yes	Tank1	1 st
Wave1_MotU	0.2	0.3	10	1.87	Yes	Tank1	1 st
Wave1_MotU_5th	0.2	0.3	10	1.87	Yes	Tank1	5 th
Wave2_Only	0.0	0.1875	6.25	2.00	No	Tank2	1 st
Wave2_Mot0	0.0	0.1875	6.25	2.00	Yes	Tank2	1 st
Wave2_MotU	0.2	0.1875	6.25	1.38	Yes	Tank2	1 st
Wave2_MotU_5th	0.2	0.1875	6.25	1.38	Yes	Tank2	5 th
Wave3_Only	0.0	0.1875	5.5	1.88	No	Tank2	1 st
Wave3_Mot0	0.0	0.1875	5.5	1.88	Yes	Tank2	1 st
Wave3_MotU	0.2	0.1875	5.5	1.27	Yes	Tank2	1 st
Wave3_MotU_5th	0.2	0.1875	5.5	1.27	Yes	Tank2	5 th

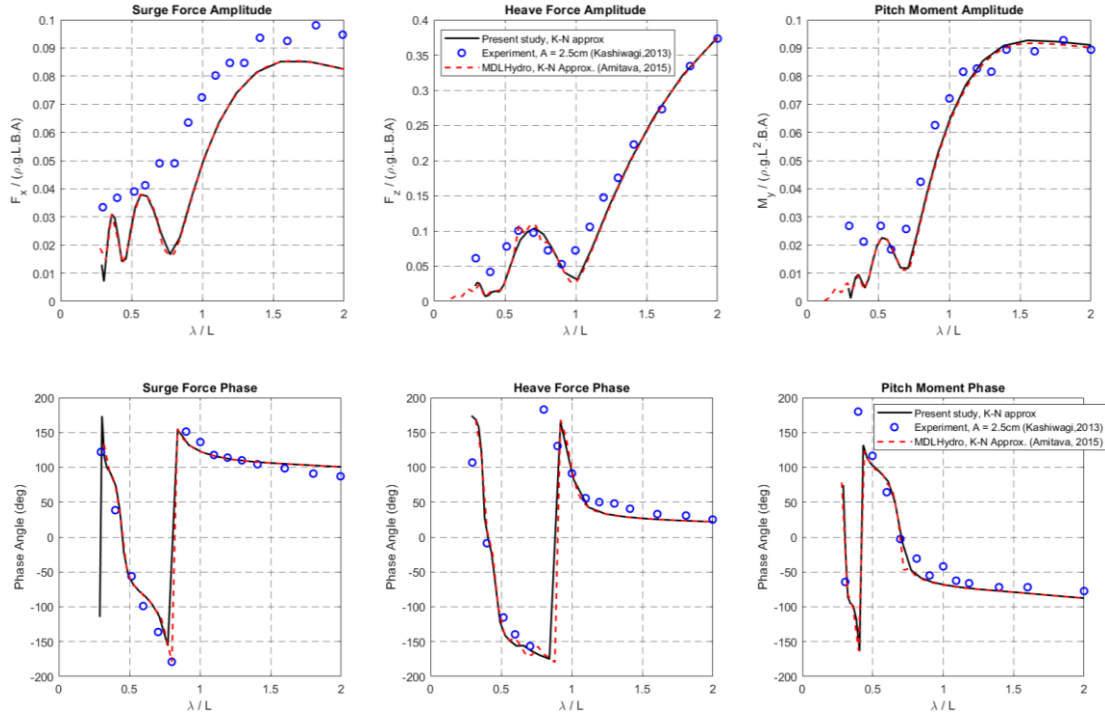


Fig. 8 Force amplitude (top) and phase (bottom) of the present study against a similar approach and experimental data for blunt Wigley hull with $F_n = 0.2$

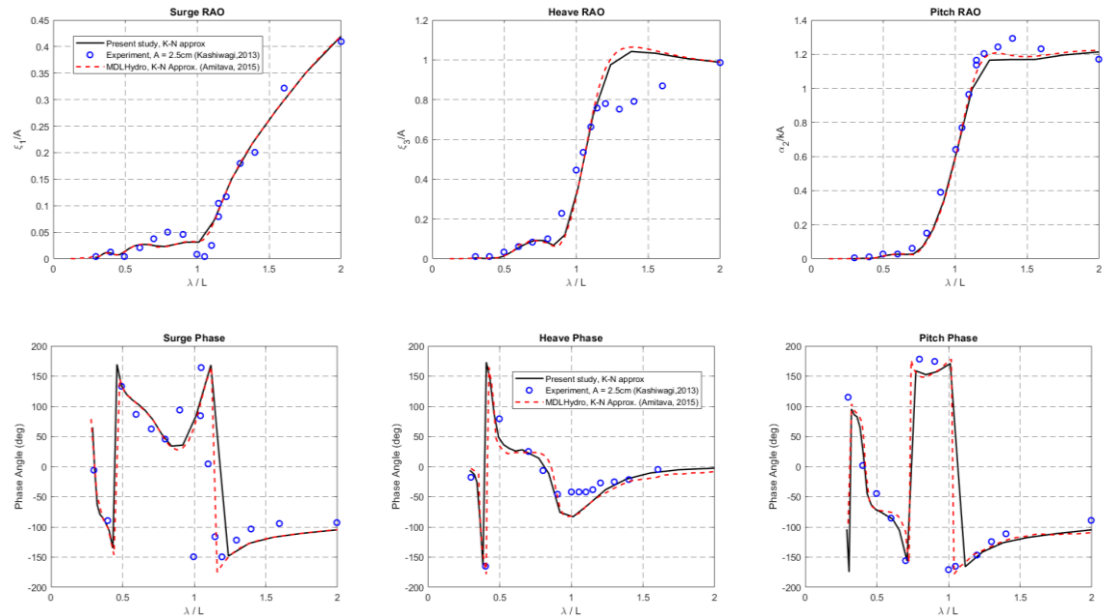


Fig. 9 RAO amplitude (top) and phase (bottom) of the present study against a similar approach and experimental data for blunt Wigley hull with $F_n = 0.2$

The body's input is considered correct when the body is at the equilibrium position, e.g., no pitch or heave static offset is observed. Note that since we use a symmetric computational domain, all the mass properties need to be halved, while all the resulting forces need to be multiplied by two. We also need to calibrate the wave height so that the comparison with other methods can be appropriately made. This calibration is done by simulating the waves without the presence of the body.

The wave slope of $H/\lambda = 0.03$ is chosen to match the experiment condition in (Kashiwagi 2013). Three wavelength conditions are simulated. $\lambda/L = 2$ is the long wave condition that is far from any resonance or cancellation frequency (i.e., easier to simulate) and $\lambda/L = 1.25$ is the pitch resonance condition in the case of $F_n = 0.2$. Lastly, $\lambda/L = 1.1$ is the maximum added resistance load condition according to Kashiwagi's experiment. In these simulations, the body is fixed in the surge direction but allowed to move in the pitch and heave directions. This setup is similar to the typical towing tank experiment with waves. A fixed body (diffraction only) case is also simulated for $\lambda/L = 2$ to validate our computational model. Since shorter waves require higher resolution and smaller total domain size than longer waves, three types of tanks are created to reduce the computational cost. Note that the wave-current interaction problem is a more complex problem than the wave-only case and might induce significant differences in the ship motion and added resistance. Therefore, we also included higher-order input wave in our wave-current CFD simulation to observe its effect. All the simulated cases can be seen in Table 2.

4. Validations and case study

4.1 BEM: Uniform flow Approximation

First, the low-fidelity numerical tool BEM-UF developed by authors is compared with other numerical simulation tools and experimental results. The modified Wigley hull with $F_n = 0.2$ is compared against a similar approach by Guha and Falzarano (2015, 2016) and experimental results by Kashiwagi (1995, 2013).

The hydrodynamic forces acting on Wigley Hull with $F_n = 0.2$ can be seen in Fig. 8 and the corresponding RAOs are given in Fig. 9. From these figures, we see a good agreement between our UF-BEM and other results for both forces and RAOs. An exception can be found in the under-predicted surge force and over-predicted heave motion by UF-BEM compared to the experiments. The former is a well-known characteristic of potential theory-based codes when simulating slender bodies, while the latter is caused by the viscous and non-linear effects near heave resonance in the experiment.

From the BEM's linear solution above, the added resistance force can be calculated by considering the time average of the surge force. The added resistance acting on the Wigley Hull with $F_n = 0.2$ can be seen in Fig. 10. From Fig. 10, our UF-BEM simulation shows consistent trends compared with other numerical results. Here, EUT stands for the enhanced unified strip theory (Kashiwagi 1995), which is similar to a standard 2D strip theory, but with additional 3D effects and surge-pitch-heave coupling effects. The present results also correlate well against published experimental results. The added resistance is a small quantity and in general hard to measure. In Kashiwagi's experiment, two different measurement methods produced different results. The present

results roughly follow the averaged values of the two measurements. The minor discrepancies near heave and pitch resonance frequencies may be attributed to non-linear and viscous effects in the experiment.

4.2 CFD: Wave height calibration and towing tank simulation

The numerical wave probe was set up to record the simulated wave elevation at ship's center of gravity location. The recorded wave-elevation is then used as the non-dimensionalization factor for forces and motions. The recorded sea-level elevation and the corresponding wave height for the 1st order input waves without uniform flow can be found in Fig. 11 and Table 3. The wave height is calculated by the zero up crossing method and then averaging them over several wave cycles (>5 cycles). Even though the wave height is slightly smaller than the target wave height, its height remains stable over a long simulation time. Furthermore, the recorded wavelength (or period) agrees well with the target wavelength. After calibrating the non-dimensionalization factor with the actual recorded wave height, the forces and motions can be appropriately compared with other numerical simulations and experimental results. The same steps were also repeated for the Stokes 5th order input waves and cases with uniform flow.

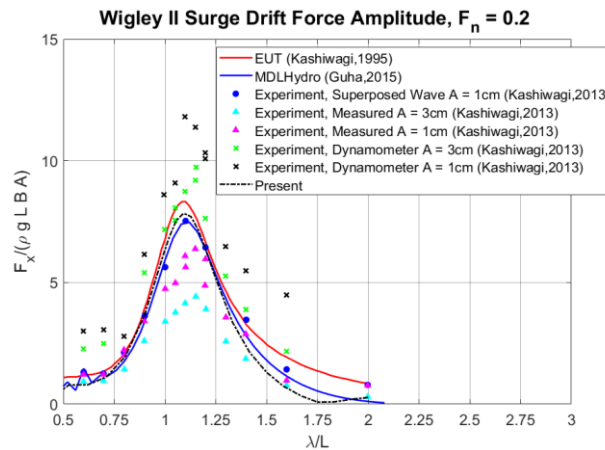


Fig. 10 Added resistance comparisons between the present BEM-UF simulation with other literatures (cf. EUT=enhanced unified strip theory)

Table 3 Recorded wave's height and period for each of λ/L cases

Case	H (m)			T (sec)		
	Simulated	Target	Diff.	Simulated	Target	Diff
Wave1_Only	0.289	0.3	-4%	2.53	2.53	0%
Wave2_Only	0.181	0.1875	-3%	2.00	2.00	0%
Wave3_Only	0.180	0.1875	-3%	1.88	1.88	0%

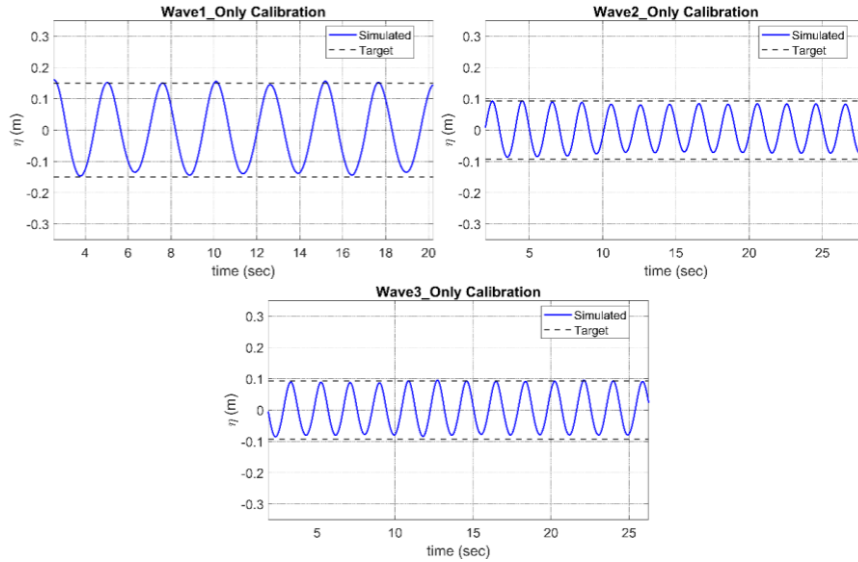


Fig. 11 Calibration of the simulated wave height and period

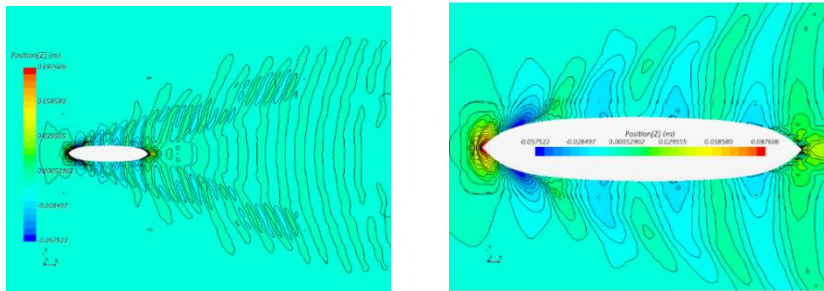


Fig. 12 Steady wave (Kelvin-ship wave) pattern (Tow Case in calm water)

Before we incorporate a rather complicated unsteady problem involving wave and current interaction, a towing tank (uniform flow simulation without waves) simulation is done to see the uniform flow effect on the steady wave's pattern (Fig. 12) and the corresponding run up along the hull (Fig. 13). As expected, the diverging Kelvin ship waves at $\sim 19^\circ$ angle from the ship's hull along with the transverse waves are observed. From Fig. 12, we can see that the sea surface elevation at the bow is larger than that of the stern. The difference in the steady wave run-up between the bow and stern coupled with the dynamic pressure caused a steady sinkage and trim on the ship, as shown in Table 4.

The comparison with Kashiwagi's (2013) experiment in Fig. 13 shows that the wave run-up along the hull agrees well with the present CFD method. Minor discrepancies at the bow location are partly caused by the run-up tracking that is done manually from the CFD results. After confirming that all of the essential features of the steady flow problem were captured correctly, we then incorporated unsteady waves into our simulations.

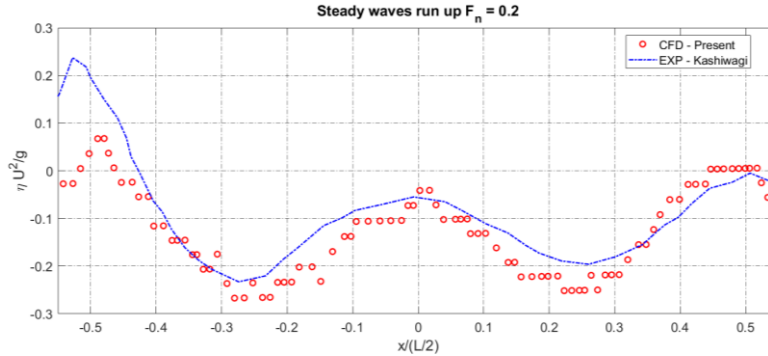


Fig. 13 Steady wave run up along the Wigley Hull

Table 4 Steady displacements

Trim (Pitch)	0.128°
Sinkage (Heave)	0.01851 m

4.3 CFD: Diffraction force validation against BEM and experiment for $\lambda/L = 2$ Case

From Fig. 8 to Fig. 10, we saw that the BEM results agreed best with the experiments at low frequencies (large wavelengths). Therefore, we choose $\lambda/L = 2$ to validate the CFD results for both wave-only and wave-uniform flow problems. The 1st order input wave is considered in the CFD simulation to properly compare with the UF-BEM.

The force and moment time-series for a fixed body (diffraction problem) are shown in Fig. 14. The experiment (Kashiwagi 2013) and the UF-BEM time series are reconstructed using simple sinusoidal functions. From the figure, both the amplitude and the frequency of the current CFD model matched well with the experiment. In the case with forward speed ($F_n = 0.2$), the encounter frequency effect is observed, and the force is increased due to the effects of additional convective pressure.

4.4 CFD: Added resistance including the effects of non-linearity in incident wave and ship motion

The cases of 1st order and 5th order input waves with a uniform flow are compared to see the effects of higher nonlinearity in incident waves. Only the cases with uniform flow close to the pitch and heave resonance frequencies are considered for this comparison. These particular cases are chosen because large ship motions and associated strong nonlinear effects are expected there. The time-series comparisons of the incident waves ($H/\lambda = 0.03$) can be seen in Fig. 15, while the corresponding ship's responses and surge forces can be seen in Figs. 16-19.

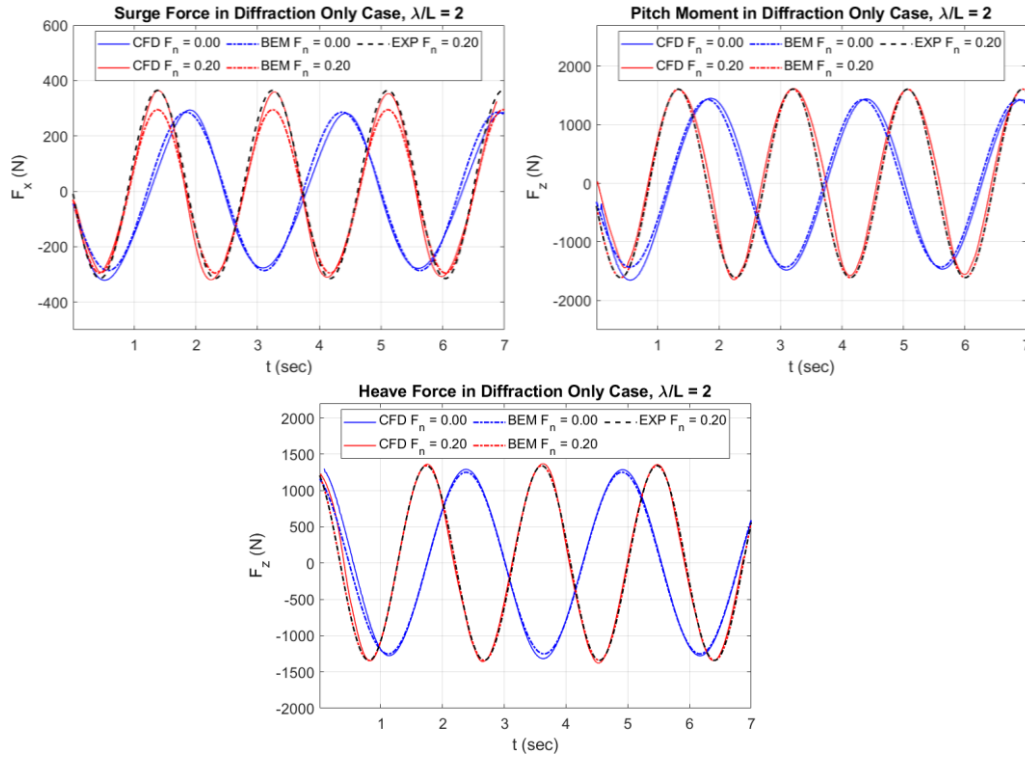


Fig. 14 Force and moment time series for $\lambda/L=2$

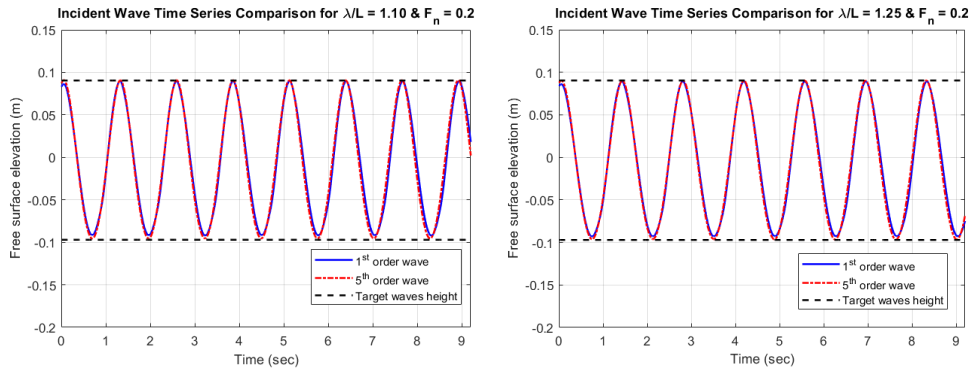


Fig. 15 Comparisons of incident-wave time series close to the velocity-inlet boundary

From Fig. 15, we can see that the 5th order waves give slightly higher crests and lower troughs than the 1st order waves, for which the applied wave steepness is $H/\lambda = 0.03$. More significant differences can be seen in the corresponding motions and forces. As can be seen in Figs. 18 and 19 the heave and pitch motions for 5th order input waves are smaller than those of the 1st order waves.

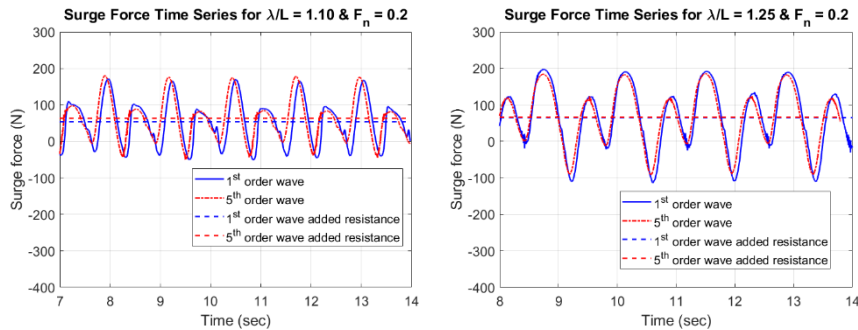


Fig. 16 Comparisons of surge force time series and the corresponding added resistance. The surge motions are restricted, while pitch and heave motions are unrestrained

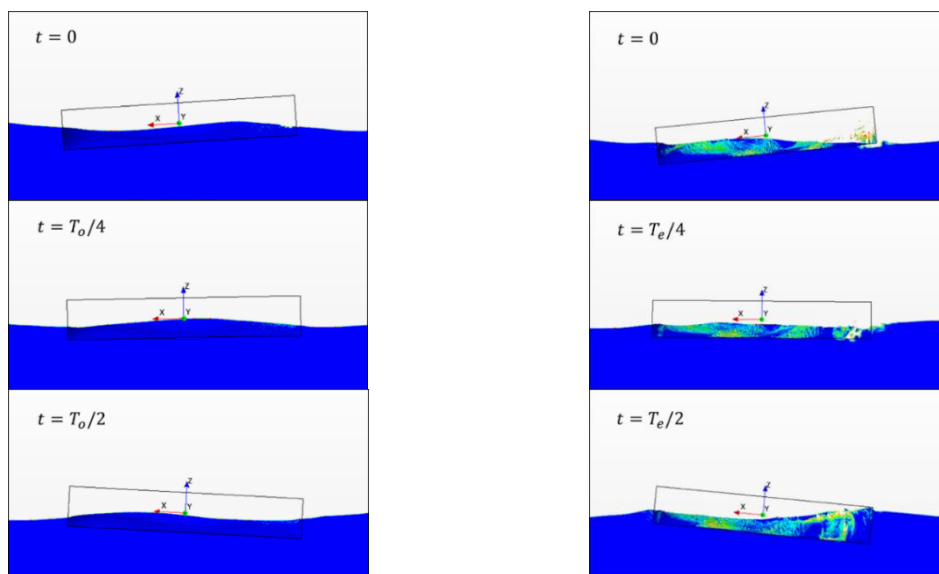
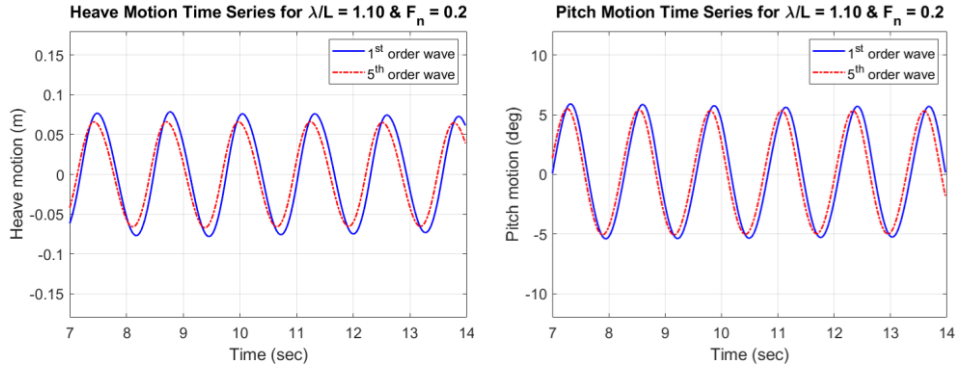
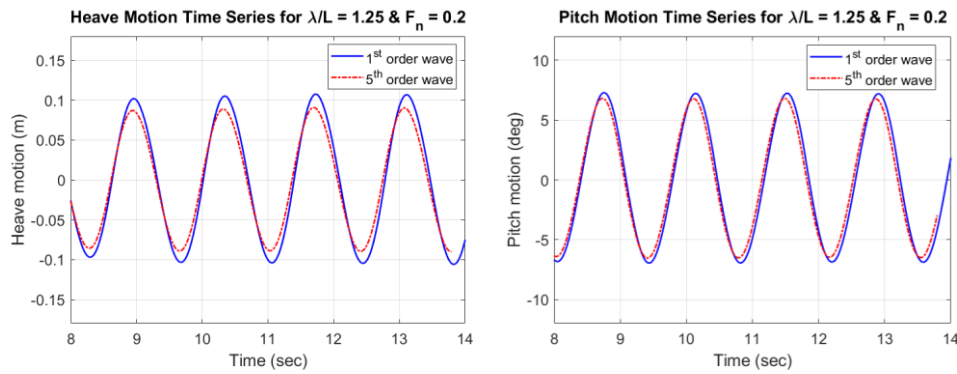


Fig. 17 Motion and free surface visualization comparisons between wave only case (left) and wave with uniform flow case (right) for $\lambda/L = 1.25$

This may happen when the phases of higher order components are opposite to that of first-order component. Fig. 16 shows that the added resistances for the 5th order waves are higher or similar compared with those of the 1st order waves. From Fig. 16, it is clear that the surge force is non-linear with forward speed ($F_n = 0.2$) even for first-order input waves. The high nonlinearity is due to spilling breaking waves occurring around the ship hull with forward speed, especially the bow side, as illustrated in Fig. 17. Bow exposure and deep submergence associated with large heave and pitch motions also contribute to the nonlinearity. We do not observe such a phenomenon in the wave-only case without forward speed (Fig. 17 left). Note that theoretically, the 5th order waves' phase speed is $(\pi H/\lambda)^2 \sqrt{g\lambda/2\pi}$ higher than the 1st order waves. This may also contribute to the nonlinear Doppler effects associated with slightly different encounter frequencies between the 1st- and 5th-order input waves.

Fig. 18 Ship's motion time series comparisons for $\lambda/L = 1.10$ Fig. 19 Ship's motion time-series comparisons for $\lambda/L = 1.25$

4.5 CFD: comparisons of ship's motion and added resistance against UF-BEM and experiments

The CFD-based ship's pitch and heave motions are compared against the experiment and UF-BEM simulation in Figs. 20 and 21. The three independent results show reasonably good agreement. The discrepancies at $\lambda/L = 1.25$ with $F_n = 0.2$ are due to large heave and pitch motions and associated breaking waves around the hull, as shown in Fig. 17. This kind of non-linearity is not considered in the UF-BEM method but was well documented in the experiment (Kashiwagi 2013). Kashiwagi also stated that these phenomena caused the added resistance experimental data to be widely spread near $\lambda/L = 1.25$, as shown in Fig. 22, in which the non-linear mean drift force (or added resistance) of the current CFD model is compared against the experimental and UF-BEM results. The added resistance was calculated by time-averaging the surge force time series over several cycles after the quasi-steady state is reached. We see that the current CFD results compare well with the UF-BEM and experiment.

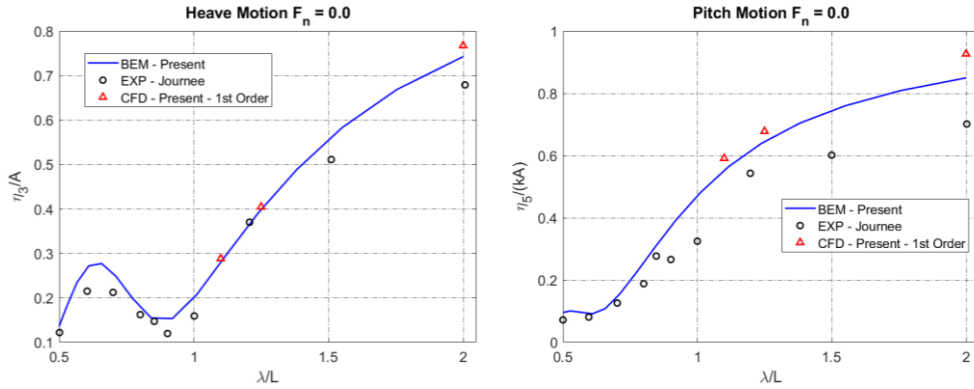


Fig. 20 Motion comparisons between the present CFD simulation with the present UF-BEM method and Journee’s experiment results (Journee 1992) for $F_n = 0.0$

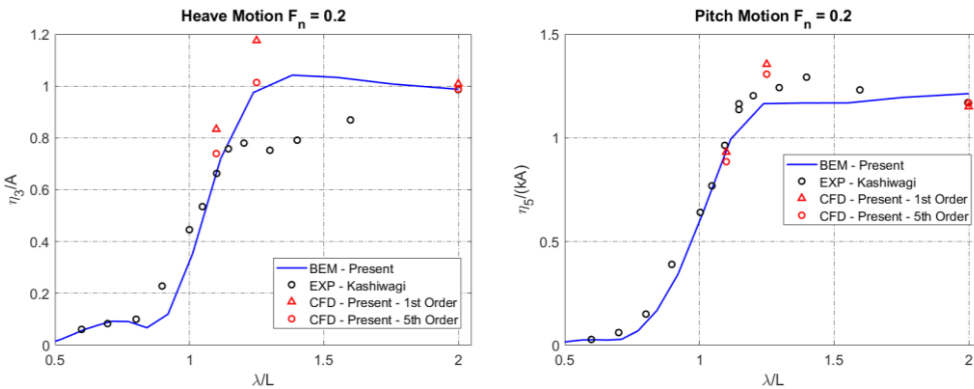


Fig. 21 Motion comparisons between the present CFD simulation with the present UF-BEM method and Kashiwagi’s experimental (Kashiwagi 2013) results for $F_n = 0.2$

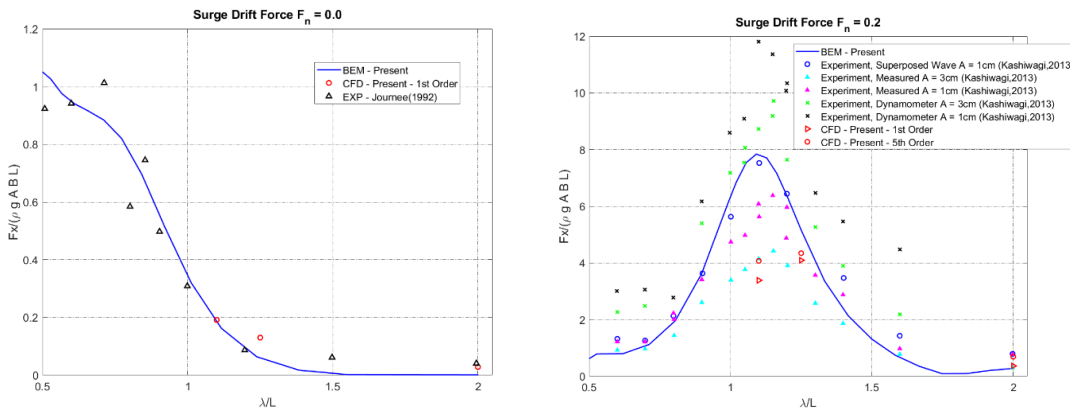


Fig. 22 Added Resistance for $F_n = 0.0$ case (left) and $F_n = 0.2$ case (right)

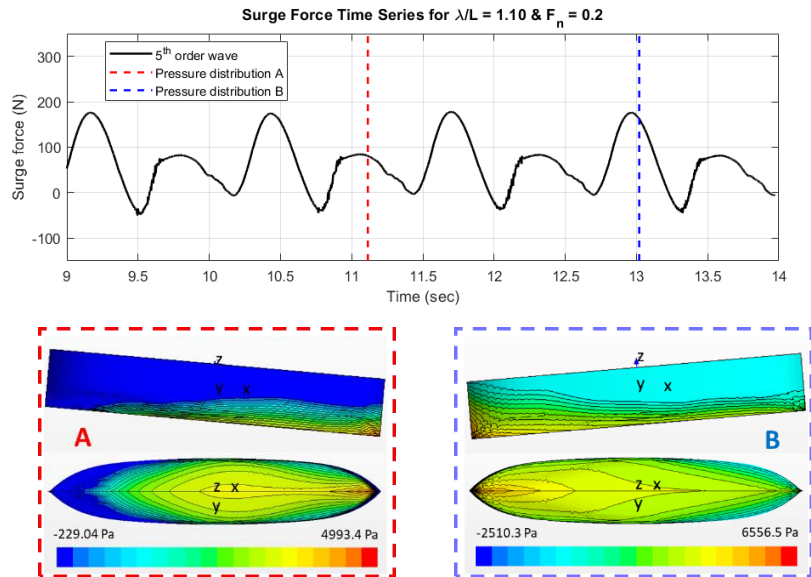


Fig. 23 Illustration of Instantaneous Non-Linear Pressure Distribution on the Hull from CFD Simulations

Despite the highly non-linear nature of the problem, the CFD simulation captured the essential features of interactions between waves and body motions with forward speed. In this regard, the 5th order input wave case gives slightly better agreement with the experimental results than the case of 1st order input wave. The strength of the CFD method is also demonstrated by its ability to capture instantaneous local pressure distribution on the hull, as can be seen in Fig. 23. These instantaneous pressure distribution from non-linear loading is useful for many engineering purposes, such as in hydro-elasticity analysis and hull-girder fatigue damage assessment.

Even though the CFD simulation could capture essential features of non-linear wave-body interactions, it requires a very high computational time and cost. For illustration, in the case involving a highly non-linear phenomenon (e.g., Fig. 17 including breaking waves), 100 CPU hours only yield 0.5 sec of simulation time. Therefore, the BEM method is still preferred in many engineering practices. The BEM is particularly useful in parametric studies for optimal design, for which many simulations need to be run with varying design parameters. Then, the CFD method can be used for the proof computation of the optimized design.

5. Conclusions

RANS-based CFD simulation was conducted for Wigley hull with (or without) forward speed to reproduce the experimental results of Kashiwagi (2013) and Journee (1992). The setup of the model with increasing complexity was explained. For quality assurance, static wave tank, wave only case, steady towing simulation, and ship in waves with (or without) forward speed were sequentially conducted to better control the overall numerical robustness. To check the sensitivity against the nonlinearity of incident waves, both 1st- and 5th-order Stokes waves were inputted and compared. An independent potential-based BEM method with uniform flow approximation was also developed

as a practical tool for preliminary design and engineering practices.

The CFD results with or without forward speed show good agreements with the BEM method and the experimental results, especially when λ/L is large. The 5th order incident wave gives slightly better agreement compared to the experimental results than the 1st order wave. The CFD simulation was able to capture the second-order mean drift loading (or added resistance) successfully. Highly non-linear dynamics involving breaking waves and large motions were observed in the CFD simulation for $\lambda/L = 1.25$ with $F_n = 0.2$ near the pitch resonance. This phenomenon is also well documented in the corresponding experiments. The CFD simulation can also capture the corresponding instantaneous non-linear pressure distribution on the hull, which is essential for hydro-elasticity analyses, including slamming and other engineering applications.

Even though the CFD simulation was able to capture most essential features of the non-linear wave-body interactions, it requires a very high computational cost. On the contrary, the UF-BEM produced comparable results, with a significantly less computational cost. Therefore, in most cases, the UF-BEM was proven to be a reliable, practical tool, except for several specific circumstances (e.g., at resonance frequency). The BEM is particularly useful in parametric studies for design optimization, for which many simulations need to be run with varying design parameters. Then, the CFD method can be used for the proof computation of the optimized design and special cases.

Acknowledgements

This work was supported by the National Research Foundation of Korea (NRF) grant funded by the Korea government (MSIT) (No. 2017R1A5A1014883).

References

- Adapco, C.D. (2020), "STAR CCM+ User's Manual", <http://www.cd-adapco.com/products/star-ccm>.
- Arjen, K., *et al.* (2020), "Development and Verification of Modeling Practice for CFD Calculations to Obtain Current Loads on FPSO", *Proceedings of the 39th International Conference on Ocean, Offshore & Arctic Engineering*.
- Bakti, F.P. and Kim, M.H. (2020), "Second Order Difference Frequency Wave-Current Loading Using Neumann-Kelvin Approximation", *Proceedings of the 39th International Conference on Ocean, Offshore & Arctic Engineering*, Virtual Online, OMAE2020.
- Bakti, F.P., Jin, C. and Kim, M.H. (2021), "Practical Approach of Linear Hydro-elasticity Effect on Vessel with Forward Speed in the Frequency Domain", *J. Fluid. Struct.*, **101**, 103204, doi: 10.1016/j.jfluidstructs.2020.103204.
- Bakti, F.P., Kim, M.H., Park, J.C. and Kim, K.S. (2016), "Comparative study of standard WC-SPH and MPS solvers for free surface academic problems", *Int. J. Offshore Polar Eng.*, **26**(3), 235-243.
- Bandringa, H. and Helder, J.A. (2020), "On the Validity of CFD for Simulating Extreme Green Water Loads", *Proceedings of the 39th International Conference on Ocean, Offshore & Arctic Engineering*, Virtual, Online, OMAE2020.
- Beck, R.F. and Loken, A.E. (1989), "Three-dimensional effects in ship relative-motion problems", *J. Ship Res.*, **33**(4), 261-268.
- Bihs, H., Kamath, A., Alagan Chella, M., Aggarwal, A. and Arntsen, Ø.A. (2016), "A new level set numerical wave tank with improved density interpolation for complex wave hydrodynamics", *Comput. Fluid.*, **140**, 191-208.
- Bouscasse, B., Bockman, A. and Ducrozet, G. (2020), "Development of A Protocol to Couple Wave and CFD

- Solvers Towards Potential Wave Kinematic Solver”, Virtual, Online, OMAE2020.
- Brard, R. (1972), “Representation of a given ship form by singularity distributions when the boundary condition on the free surface is linearized”, *J. Ship Res.*, **16**(1), 79-92.
- Celebi, M.S., Kim, M.H. and Beck, R.F. (1998), “Fully nonlinear 3D numerical wave tank simulations”, *J. Ship Res.*, **42**(1), 33-45.
- Flock, A.K., Guildenbecher, D.R., Chen, J., Sojka, P.E. and Bauer, H.J. (2012), “Experimental statistics of droplet trajectory and air flow during aerodynamic fragmentation of liquid drops”, *Int. J. Multiphase Fl.*, **47**, 37-49.
- Guha, A. and Falzarano, J. (2015), “The effect of hull emergence angle on the near field formulation of added resistance”, *Ocean Eng.*, **105**, 10-24.
- Guha, A. and Falzarano, J. (2016), “Estimation of hydrodynamic forces and motion of ships with steady forward speed”, *Int. Shipbuild. Progress*, **62**(3-4), 113-138.
- Hadzic, H. (2005), “Development and Application of a Finite Volume Method for the Computation of Flows Around Moving Bodies on Unstructured, Overlapping Grids”, *Dissertation*, Technische Universit“at Hamburg.
- Heilskov, N.F. and Petersen, O.S. (2016), “Non-Linear 3D Hydrodynamics of Floating Wind Turbine Compared Against Wave Tank Tests”, *Proceedings of the 35th International Conference on Ocean, Offshore & Arctic Engineering*, Busan, South Korea.
- Irkal, M.A.R., Nallayarasu, S. and Bhattacharyya, S.K. (2016), “CFD approach to roll damping of ship with bilge keel with experimental validation”, *Appl. Ocean Res.*, **55**, 1-17.
- Islam, H., Rahaman, M. and Akimoto, H. (2019), “Added Resistance Prediction of KVLCC2 in Oblique Waves”, *Am. J. Fluid Dynam.*, **9**(1), 13-26.
- Jiao, J. and Huang, S. (2020), “CFD simulation of ship seakeeping performance and slamming loads in Bi-directional cross wave”, *J. Mar. Sci. Eng.*, **8**(5), 1-24.
- Jin, Y., Chai, S., Duffy, J., Chin, C. and Bose, N. (2017), “URANS predictions of wave induced loads and motions on ships in regular head and oblique waves at zero forward speed”, *J. Fluid. Struct.*, **74**, 178-204.
- Journee, J.M.J. (1992), “Experiments and calculations on 4 Wigley hull forms in head waves”, *Delft University of Technology Report*, no. May 1992, 1-99.
- Kashiwagi, M. (1995), “Prediction of Surge and its Effect on Added Resistance by Means of the Enhanced Unified Theory”, *Trans West-Japan Society of Naval Architects*, **89**, 77-89.
- Kashiwagi, M. (2013), “Hydrodynamic study on added resistance using unsteady wave analysis”, *J. Ship Res.*, **57**(4), 220-240.
- Kim, J., O'Sullivan, J. and Read, A. (2012), “Ringing analysis of a vertical cylinder by Euler overlay method”, *Proceedings of the 31st International Conference on Ocean, Offshore & Arctic Engineering*, Rio de Janeiro, Brazil.
- Kim, K. H., and Kim, Y. (2010), "Comparative study on ship hydrodynamics based on Neumann-Kelvin and double-body linearizations in time-domain analysis," *International Journal of Offshore and Polar Engineering*, vol. 20, no. 4, pp. 265-274.
- Kim, S.J. and Koo, W. (2019), “Development of a three-dimensional fully non-linear potential numerical wave tank for a heaving buoy wave energy converter”, *Math. Probl.Eng.*, **2019**(1).
- Muzaferija, S. and Peric, M. (2017), “Computation of free-surface flows using interface-tracking and interface- capturing methods”, *Fluid Dynamics and Ship Theory Section*, Technical University of Hamburg, Hamburg.
- Ogilvie, T. and Tuck, E. (1969), “A rational strip theory of ship motions: part I”, *Naval Ship Systems Command General Hydromechanics Research Program Subproject SR 009 01 01 Report*, no. N00014-67-A-0181-0016.
- Orihara, H. (2011), “Comparison of CFD simulations with experimental data for a tanker model advancing in waves”, *Int. J. Naval Archit. Ocean Eng.*, **3**(1), 1-8.
- Papanikolaou, A. and Schellin, T. (1992), “A three-dimensional panel method for motions and loads of ships with forward speed”, *Ship Technol. Res. (Schiffstechnik)*, **39**(4), 145-155.
- Sadat-Hosseini, H., Wu, P.C., Carrica, P.M., Kim, H., Toda, Y. and Stern, F. (2013), “CFD verification and validation of added resistance and motions of KVLCC2 with fixed and free surge in short and long head

- waves”, *Ocean Eng.*, **59**, 240-273.
- Salvesen, N., Tuck, E. and Faltinsen, O. (1970), “Ship motions and sea loads”, *The Society of Naval Architects and Marine Engineers*, **78**, 250-287.
- Vigsnes, J.T. (2018), “Seakeeping Analysis Comparison between Viscous and Inviscid CFD”, *Dissertation*, Norwegian University of Science and Technology, Dept. of Marine Engineering.
- White, F.M. (2006), *Viscous fluid flow*, 3rd ed. New York: McGraw-Hill.
- Wilcox, D.C. (1998), *Turbulence Modeling for CFD*, 2nd ed. La Canada, California: DCW Industries.
- Wu, C.S., Zhou, D.C., Gao, L. and Miao, Q.M. (2011), “CFD computation of ship motions and added resistance for a high speed trimaran in regular head waves”, *Int. J. Naval Architect. Ocean Eng.*, 3(1), 105-110.

PL